A&A 477, 55–66 (2008)
DOI: 10.1051/0004-6361:20077591

Astronomy & Astrophysics

EROs found behind lensing clusters⋆

II. Empirical properties, classification, and SED modelling based on multi-wavelength observations⋆⋆

A. Hempel[1], D. Schaerer[1,3], E. Egami[2], R. Pelló[3], M. Wise[4], J. Richard[5,3], J.-F. Le Borgne[3], and J.-P. Kneib[6]

[1] Observatoire de Genève, 51 chemin des Maillettes, 1290 Sauverny, Switzerland
e-mail: [angela.hempel;daniel.schaerer]@obs.unige.ch
[2] Steward Observatory, University of Arizona, 933 North Cherry Street, Tucson, AZ 85721, USA
[3] Observatoire Midi-Pyrénées, Laboratoire d'Astrophysique, UMR 5572, 14 Avenue E. Belin, 31400 Toulouse, France
[4] Astronomical Institute Anton Pannekoek, Kruislaan 403, 1098 SJ Amsterdam, The Netherlands
[5] Caltech Astronomy, MC105-24, Pasadena, CA 91125, USA
[6] OAMP, Laboratoire d'Astrophysique de Marseille, UMR 6110, traverse du Siphon, 13012 Marseille, France

Received 3 April 2007 / Accepted 30 August 2007

ABSTRACT

Aims. We study the properties and nature of extremely red galaxies (ERO, $R-K \geq 5.6$) found behind two lensing clusters and compare them with other known galaxy populations.
Methods. New HST/ACS, Spitzer (IRAC and MIPS), and Chandra/ACIS observations of the two lensing clusters Abell 1835 and AC114 have been obtained, combined with our earlier optical and near-IR observations and used to study EROs in these deep fields.
Results. We have found 6 and 9 EROs in Abell 1835 and AC114. Several (7) of these objects are undetected up to the I and/or z_{850} band, and are hence "optical" drop-out sources (at a 3σ limit). The photometric redshifts of most of our sources (80%) are $z \sim 0.7$–1.5. According to simple colour–colour diagrams, the majority of our objects would be classified as hosting old stellar populations ("ellipticals"). However, there are clear signs of dusty starbursts for several among them. These objects correspond to the most extreme ones in $R-K$ colour. After correcting for lens magnification, we estimate a surface density of (0.97 ± 0.31) arcmin^{-2} for EROs with $(R-K \geq 5.6)$ at $K < 20.5$. As in earlier studies, an overlap of different populations is found. Among our 15 EROs 6 (40%) also classify as distant red galaxies. Eleven of 13 EROs (85%) with available IRAC photometry also fulfil the selection criteria for IRAC selected EROs (IEROs) of Yan et al. (2004, ApJ, 616, 63). SED modelling shows that ∼36% of the IEROs in our sample are luminous or ultra-luminous infrared galaxies ((U)LIRG). Some very red DRGs are found to be very dusty starbursts, even (U)LIRGs. No AGNs is found, although faint activity cannot be excluded for all objects. From mid-IR and X-ray data, 5 objects are clearly classified as starbursts. The derived properties are quite similar to those of DRGs and IEROs, except for 5 extreme objects in terms of colours, for which a very high extinction ($A_V \gtrsim 3$) is found.

Key words. galaxies: high-redshift – galaxies: starburst – infrared: galaxies – galaxies: evolution

1. Introduction

Since their discovery in the late 1980s (Elston et al. 1988, 1989), extremely red objects (EROs) have attracted serious attention. These first detections were initially presumed to be high-redshift ($z > 6$) galaxies in a star-forming phase (Elston et al. 1988). Multi-colour, follow-up observations later identified these objects as luminous galaxies at $z = 0.8$, dominated by an old stellar population (Elston et al. 1989). The detection of two bright ($K \gtrsim 18.4$) extended objects (HR10 & HR14) with $(I-K)$ colours near 6.5 by Hu & Ridgway (1994) highlighted the difficulty of classifying these galaxies. When first discovered, HR10 and HR14 were interpreted as ellipticals at $z \sim 2.4$. Subsequent spectroscopic and morphological observations indicated that HR10 is not a quiescent elliptical galaxy, but rather a bright interacting galaxy at $z = 1.44$ (Graham & Dey 1996; Stern et al. 2006).

In general there are two main scenarios that would produce a spectral energy distribution that is red enough to satisfy the established colour criteria for EROs (e.g. $R-K > 5$–7, $I-K > 4$–6), either due to an old passively evolved population or by extreme dust reddening as found in star bursts (Cowie et al. 1994; Cimatti et al. 1999; Daddi et al. 2002; Georgakakis et al. 2006) in a redshift range of $1 \lesssim z \lesssim 2$. A number of review articles discuss various aspects related to this topic (e.g. McCarthy 2004; Ferguson et al. 2000).

The abundance of massive old ellipticals in particular poses a strong test for the two competing scenarios of elliptical galaxy

⋆ Tables 1–6 are only available in electronic form at
http://www.aanda.org

⋆⋆ Based on observations collected at the Very Large Telescope (Antu/UT1), European Southern Observatory, Paranal, Chile (ESO Programs 69.A-0508, 70.A-0355, 73.A-0471), the NASA/ESA *Hubble Space Telescope* obtained at the Space Telescope Science Institute which is operated by AURA under NASA contract NAS5-26555, the Spitzer Space Telescope, which is operated by the Jet Propulsion Laboratory, California Institute of Technology under NASA contract 1407, and the Chandra satellite.

formation: early assembly ($z_f > 2$–3), e.g. by monolithic collapse, and passive luminosity evolution thereafter (PLE models) (Tinsley & Gunn 1976; Pozzetti et al. 1996), or hierarchical merging of smaller sized objects (White & Rees 1978; Kauffmann et al. 1993; Somerville et al. 2001). Observational evidence has been found for both scenarios: several surveys have detected a deficit of ellipticals at $z > 1$, supporting the hierarchical merging models (Roche et al. 2003; Kitzbichler & White 2006), while others are consistent with PLE (Im et al. 2002; Cimatti et al. 2002; Somerville et al. 2004).

However, in recent years the hierarchical merging scenario in a ΛCDM universe has been established as the favoured model. Nevertheless, the vast number of different renditions leaves room for dramatically different predictions regarding critical parameters like the number density of massive galaxies at specific times (Fontana et al. 2004; Treu et al. 2005, and references therein).

The picture is complicated by the results of numerous morphological studies on EROs, which assigns a large fraction of EROs to disk galaxies at somewhat lower redshifts (Yan & Thompson 2003; Gilbank et al. 2003; Moustakas et al. 2004). In addition, a small fraction of EROs could also be active galactic nuclei (AGNs), as shown by deep XMM and Chandra data (Alexander et al. 2002; Roche et al. 2003; Brusa et al. 2005).

With the increasing number of large-scale surveys like UKIDSS (Simpson et al. 2006) and others it became clear that other means than spectroscopy are needed in order to classify to which of the two major galaxy populations the large number of EROs belong. These could be either combinations of *RIJHK* (Pozzetti & Mannucci 2000; Bergström & Wiklind 2004) colours or the use of near and mid-infrared bands (Wilson et al. 2004).

Independently of which exact colour criteria has been used, all EROs have at least one mutual property, their faintness at optical wavelengths causing limitations to the accuracy of photometric redshift estimates and other parameters derived from SED features. To increase the apparent brightness of EROs, we use the natural magnification effect provided by massive galaxy clusters. This method has been applied successfully for the investigation of other faint sources, like Lyman break galaxies (Pettini et al. 2000; Swinbank et al. 2007), faint SCUBA sources (Smail et al. 1998; Ivison et al. 2001), and EROs (Smith et al. 2002; Takata et al. 2003).

In the present study we systematically select EROs in the fields of the two lensing clusters Abell 1835 and AC114, based on observations obtained by Richard et al. (2006) and new ACS/HST, Spitzer, and Chandra observations. These are used to discuss their empirical properties and their nature and to derive physical parameters like photometric redshift, extinction, star-formation rates, and stellar population properties. Several of these objects were found earlier in our H-band selected sample of optical drop-out objects constructed for the search of high-redshift galaxies (see Richard et al. 2006). The ERO subsample from that paper is analysed in detail in Schaerer et al. (2007).

Throughout this paper we adopted the following cosmology: $\Omega_m = 0.3$, $H_0 = 70$ km s^{-1} Mpc^{-1} in a flat universe. All magnitudes are given in the Vega system if not stated otherwise.

2. Observations and data reduction

The observations described here are part of multi-colour observations on two galaxy clusters, AC114 and Abell 1835, which have well-known lensing properties. An extensive description of the initial observations (optical and near-infrared data) and the available data can be found in Richard et al. (2006). Exposure time, limiting magnitudes, and more characteristics can be found in Table 1.

The near-infrared data (SZ, J, H and K_s) were obtained with the Infrared Spectrometer and Array Camera (ISAAC) located on the VLT-UT1 (FOV 2.5 acrmin × 2.5 arcmin with a pixel size of 0.148 arcsec). The optical data for Abell 1835 (*VRI*) are archive data from the CFHT12k camera at CFHT (Czoske et al. 2003), and those for AC114 (*UBVRI*) were taken from Campusano et al. (2001).

2.1. ACS data

New z-band (F850LP, denoted z_{850} hereafter) imaging was obtained with the ACS camera onboard HST in November 2004 (AC114) and July 2005 (Abell 1835). The total observing time for AC114 and Abell 1835 were 9184 and 9110 s, respectively. While the AC114 field is centred at the central cluster galaxy, Abell 1835 was observed off centre in order to avoid bright sources north of the cluster. To reduce both data sets we used the IRAF/Pyraf package *multidrizzle* on post-calibrated data[1].

For the calculation of the 1σ detection limit, we applied the same method as for all other bands (see Richard et al. 2006): measuring the corresponding standard deviation of the flux in randomly distributed circular apertures of 1.5 arcsec diameter (approx. 3000). None of the aperture positions lies within 3 arcsec to its closest neighbour or to sources that have at least a 3σ detection.

2.2. IRAC and MIPS data

The 3.6, 4.5, 5.8, and 8.0 μm images were obtained using the Infrared Array Camera (IRAC; Fazio et al. 2004), while the 24 μm images were obtained using the Multi-band Imaging Photometer for *Spitzer* (MIPS; Rieke et al. 2004), both onboard the *Spitzer* Space Telescope (Werner et al. 2004). The instruments, data, and reduction procedures are described in Egami et al. (2006).

2.3. Chandra

Both Abell 1835 and AC114 were observed previously by *Chandra*, AC114 was observed once for a total exposure of 75 ks (OBSID 1562). A comprehensive analysis of the cluster X-ray properties based on this dataset has been published previously in De Filippis et al. (2004). In the case of Abell 1835, two short archival observations are available (OBSIDs 495 and 496), as well as a deep 200 ks GO observation (OBSIDs 6880, 6881, and 7370) obtained as part of this program. All available data were reprocessed using CIAO 3.2 and the latest calibration files available in CALDB 3.0. Standard screening was applied to all event files to remove bad grades, bad pixels, and background flares. After standard cleaning, the resulting net exposures were 73 and 224 ks for AC114 and Abell 1835, respectively.

Bright X-ray point sources in the fields of AC114 and Abell 1835 were identified using the CIAO tool `wavdetect`. No bright X-ray point sources were detected within 5 arcsec of the ERO source positions. To determine flux upper limits, source spectra were extracted in a 2 arcsec radius aperture around each ERO source position. This aperture captures virtually all of the Chandra PSF over the range of relevant off-axis angles. The local background for each source was determined using an

[1] For details see `http://stsdas.stsci.edu/pydrizzle/multidrizzle`

annular aperture from 2–4 arcsec surrounding the source aperture. Count-weighted detector response (RMFs) and effective area (ARFs) files were created for each extraction region using the CIAO tools `mkacisrmf` and `mkwarf`, including the temporal, spectral, and spatial dependence of the ACIS filter contaminant. For Abell 1835, source spectra and matching background, RMF, and ARF files were produced for each OBSID separately and then fit jointly during the spectral analysis. This analysis is discussed in more detail in Sect. 3.3. All spectral analysis was done using the ISIS Houck & Denicola (2000) spectral fitting package and the XSPEC model library.

In the case of Abell 1835, spectra from all 5 observations (2 archival datasets and 3 datasets as part of our program) were extracted for each source and fit simultaneously. Each dataset was individually reprocessed using CIAO 3.2 and calibration files available in CALDB 3.0.

3. Photometry

3.1. Optical and near-infrared

As our objective is to study EROs, we proceeded by identifying sources in the ISAAC K_s-band image using SExtractor2.2.2 (Bertin & Arnouts 1996)[2] and requiring a 3σ threshold above the background in at least 4 pixels. The photometry in all ISAAC images ($SZJH$) was done in the double-image mode of SExtractor2.2.2, using the K_s-band image as reference.

Note that our earlier work on these clusters, including the identification of optical drop-out EROs, was done on an H-band selected sample (Richard et al. 2006). In contrast to Richard et al. (2006), we used AUTO_MAG instead of aperture photometry, mainly because some of our EROs are quite extended and using large enough apertures might induce additional problems due to the close proximity of other sources. As a consequence, we used the error provided by SExtractor and not one based on the S/N characteristics in a fixed aperture (see Richard et al. 2006). However, comparing the photometric errors for the EROs already described in Richard et al. (2006), we found no significant difference between the photometric error based on aperture photometry or AUTO_MAG. For the SED fitting a minimum photometric error of 0.1 mag was generally used.

For objects that were not detected in a specific band, we substituted the detection limit for a 3σ detection threshold as apparent magnitude. Using our ERO criterion of $(R-K_s) \geq 5.6$, we automatically compiled a catalogue of ERO candidates. The $RJHK$ image of each of these candidates was then examined by eye in order to reject spurious detections, e.g. at the edge of the image or candidates blended with another source. This procedure resulted in the identification of 6 EROs in Abell 1835 and 9 in AC114. In Richard et al. (2006), we found 7 and 1 resolved objects with extremely red optical to near-infrared colours in Abell 1835 and AC114, respectively, which qualified as ERO. Five of the objects in Abell 1835 cannot be classified as ERO if we use the 3σ detection limit for R-band non-detections. Dismissing the optical drop-out criteria applied in that paper and using a different photometry (see above), we now find 4 additional EROs in Abell 1835 and 8 in AC114. The postage stamps of our objects are shown in Figs. 1 and 2.

As result of the higher spatial resolution of ACS, A1835-#319 appears resolved into two sources. It remains to be seen, whether or not we are looking at physically distinct sources, or objects which are gravitational bound. For the adopted cosmology the projected distance of 0.213 arcsec of the two components of #319 corresponds to 1.7 kpc, assuming a source redshift of 2.5 as indicated from their SED analysis (Schaerer et al. 2007). These estimates are based on the angular distance without correction for lensing and hence state an upper limit for the distance between the two components.

For the astrometry we used standard stars from the ESO-USNO-A2.0 catalogue to obtain correct coordinates (J2000). All coordinates are based on their position in the K_s-band image.

3.2. IRAC and MIPS photometry

The IRAC photometry used a circular aperture with a radius of 2.″4 with a sky background annulus of 2.″4–7.″2 in radius. The point-source aperture corrections were applied, which were 1.213, 1.234, 1.379, and 1.584 at 3.6, 4.5, 5.8, and 8.0 μm, respectively, based on the IRAC Data Handbook.

The MIPS 24 μm photometry used a circular aperture with a radius of 6″ with a sky background annulus of 6″–13″ in radius. The corresponding point-source aperture correction was 1.698 based on the MIPS instrument web site. For several EROs, we encountered severe blending problems (see Table 4), so these were not included in our discussion nor in Figs. 5 and 6. The source positions at 5.8 and 8 μm are slightly displaced from those at shorter wavelengths. Therefore, there is a possibility that the emission at >4.5 μm is not related to the ERO but to the fainter sources to the east.

3.3. Chandra photometry

None of the ERO sources were detected in the fields of AC114 and A1835. To place upper limits on the possible X-ray emission from the EROs, we compared the extracted spectra discussed in Sect. 2.3 at each ERO source position with a number of spectral models for the assumed underlying spectral energy distribution. These flux distributions were fit to a simple power-law model including foreground Galactic absorption. Such a model would be expected if the intrinsic X-ray spectra of the ERO was dominated by AGN emission. The absorbing column was fixed to the Galactic value for each cluster and held fixed during the fitting procedure. Due to the low number of counts associated with a given source, the spectral index of the power-law model was similarly held fixed during the fitting. Values of 1.0, 1.4, and 2.0 were considered for the photon spectral index and different energy ranges were considered for comparison with other data from the literature. The resulting flux limits for each ERO source (at a 3-sigma level) are listed in Table 5.

4. Empirical properties of our EROs and comparisons with other samples

As mentioned above, our search for EROs with $R - K_s > 5.6$ in Abell 1835 and AC114 has yielded 15 (16) objects in total, depending on whether sources appearing as double in the ACS images are counted. Two of the additional EROs (#347 & #532) detected in Abell 1835 were not included in Richard et al. (2006) and Schaerer et al. (2007) due to the additional selection criterion of optical non-detection imposed in these papers. Two more objects (#319 & #676) were previously excluded during the eye-examination (as described in Sect. 3). Six of the additional EROs in AC114 can be detected in R using the initial detection threshold of 1σ, hence were not included in Richard et al. (2006) or Schaerer et al. (2007). The remaining two new sources were

[2] This software is freely available from `http://terapix.iap.fr/`

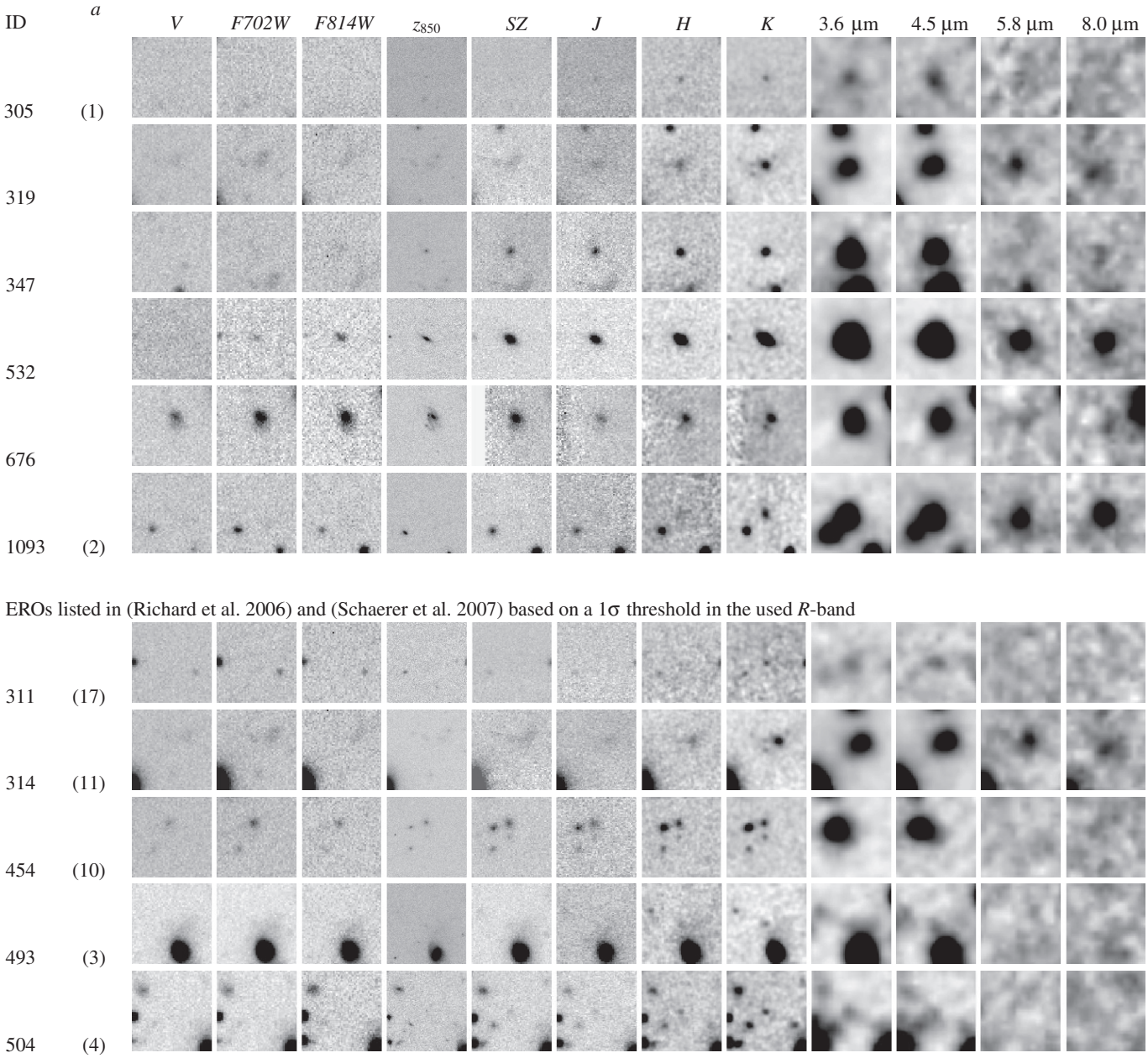

Fig. 1. Close-up images of EROs found in Abell 1835. Each of the panels is 20 arcsec across, North is up and East is left. Source number 1093 is the NIR-counterpart of the sub-mm source SMMJ14009+0252. [a] The numbers in brackets refer to Richard et al. (2006) and Schaerer et al. (2007).

previously excluded during the visual examination, either due to a close bright object (#1006) or because of its position at the edge of the image (#1087).

We now discuss the properties of the EROs and compare them to other samples and to related objects. At this point we note that we do not differentiate between the various K-band filters.

4.1. EROs with very red R–K_s colours

Figures 3 and 4 show some of the photometric properties of our EROs in comparison to other samples. These figures show that there are some sources, both in Abell 1835 and AC114, that have very red colours both with $(R - K_s) \gtrsim 7$ and $(I - K_s) \gtrsim 6$ (adopting 3σ limits for the non-detected bands). Such relatively bright ($K_s < 20.3$) and red sources were not found in other surveys, e.g. HUDF (Yan et al. 2004), MUNICS (Longhetti et al. 2005), and GOODS-MUSIC (Grazian et al. 2006, 2007), although their depth is sufficient for detecting such red objects. However, Sawicki et al. (2005) report 5 EROs with $R - K_s > 7.0$ at similar magnitudes to our objects. The origin of these apparent differences is not clear. However, it has to be recognised that all samples except GOODS-MUSIC are relatively small and lack statistical significance.

4.2. ERO classification (starburst vs. old population)

Although colours alone cannot provide the same strong constraints on their nature and photometric redshift as SEDs or spectra, we used the colour-based classification scheme introduced by Pozzetti & Mannucci (2000) for a first classification of our sample. This photometric method uses the $(R - K)$ vs.

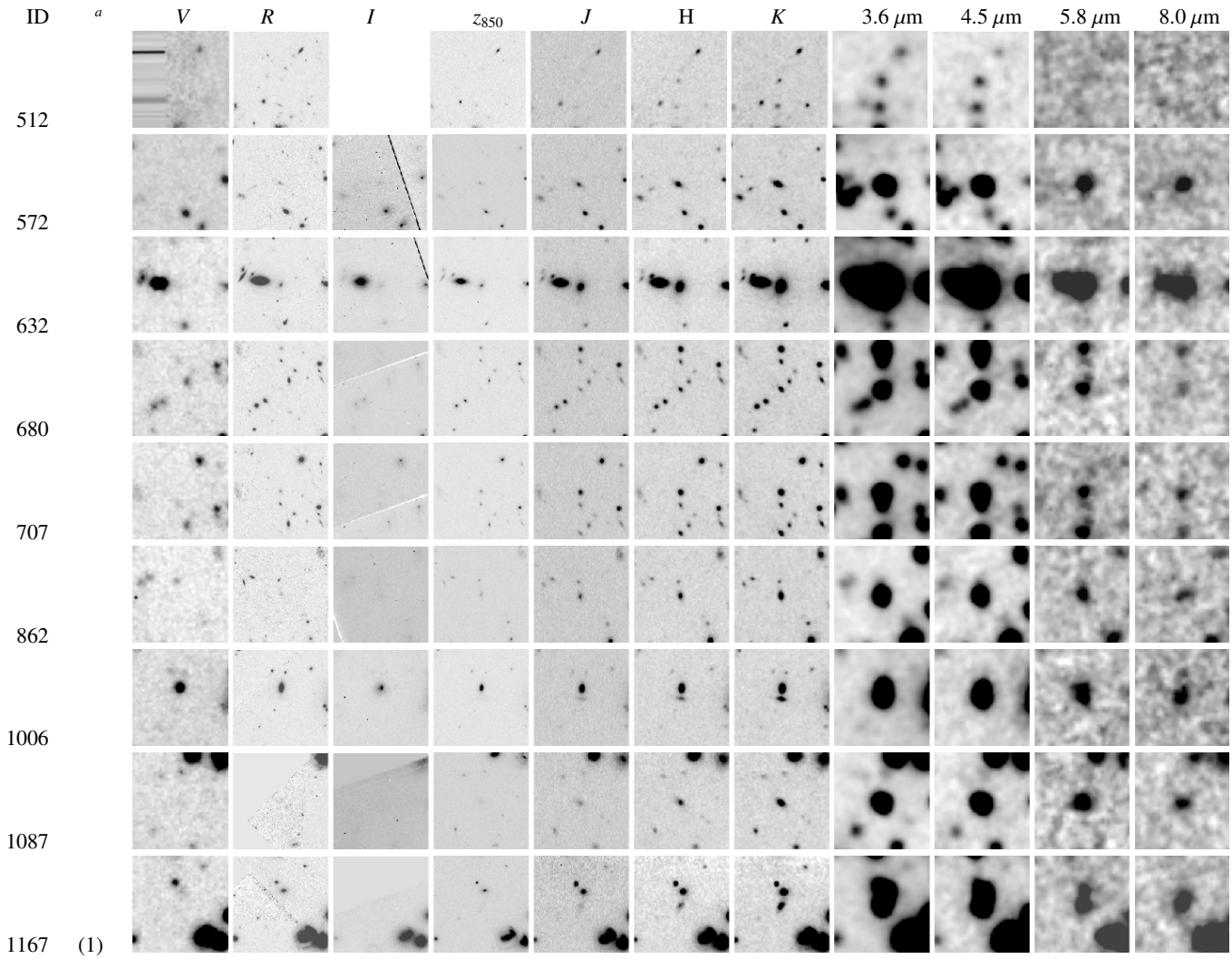

Fig. 2. Same as Fig. 1 for the EROs in AC114. Source 512 lies outside the recorded *I*-band image.

$(J - K)$ colour plane to separate between galaxies with old stellar populations and dusty starbursts, assuming a redshift range of $1 \lesssim z \lesssim 2$. The corresponding colour-colour diagram of our EROs is shown in Fig. 3. For comparison we have also included EROs found by the MUNICS survey (Longhetti et al. 2005), IEROs in the HUDF (Yan et al. 2004), and a sample of EROs found by Takata et al. (2003) in the field of the submillimeter source SMM J04542-0301 (cluster MS0451.6-0305).

However, if taking other information into account, this simple classification scheme does not always yield consistent results. For example, several objects classified as "elliptical" on the basis of Fig. 3 are detected at 24 μm – incompatible with an old and dust-free population. Furthermore, the SED analysis (cf. Sect. 5) of these objects and several other objects in the "ellipticals" region shows that they are more likely dusty bursting objects. Nevertheless, one has to keep in mind that many of our objects have colours close to the separation line (as calculated by Pozzetti & Mannucci 2000) and that the gap between both populations is approximately 0.3 mag wide (Fig. 3). In this respect, many of our less extreme EROs could also be classified as starburst. Also, Pozzetti & Mannucci include exponential declining SFH up to decay times of $\tau \sim 0.3$ Gyr in their models of evolved populations, while we only consider instantaneous burst scenarios for evolved populations.

4.3. Redshift estimates for EROs with IRAC and/or MIPS detection

According to Wilson et al. (2004), an ERO selection equivalent to $R - K > 5$ (less red than our colour threshold) using the IRAC 3.6 μm band would require an $R - [3.6]$ colour redder than 6.6 (Vega) or 4.0 (*AB* magnitude). All our IRAC – detected EROs fulfil this criterion (generally $R - [3.6]_{\rm Vega} > 7.4$). The combination of $K_{\rm s}$-band and IRAC bands also allow a rough estimate of redshift, based on the shift of the 1.6 μm bump. This spectral feature can be found in the spectra of all galaxies with the exception of AGN-dominated SEDs, so it can be used to estimate the photometric redshift (Sawicki 2002). In practice, using colour criteria of $(K - [3.6])_{\rm Vega} > 0.9$ and $([3.6]–[4.5])_{\rm Vega} < 0.47$ limits the photometric redshift interval to $0.6 < z < 1.3$, while $(K - [3.6])_{\rm Vega} > 0.9$ and $([3.6]–[4.5])_{\rm Vega} > 0.47$ should select galaxies with redshifts above 1.3, according to Wilson et al. (2004). The corresponding colour-colour plot showing our objects and comparison samples is given in Fig. 5. All objects except #305 satisfy this $K - [3.6]$ criterion. From their red ([3.6]–[4.5]), we expect that #1093 is clearly above $z > 1.3$. In fact, detailed SED modelling yields photometric redshift estimates of $z_{\rm phot} \sim 2.0$ and 2.8–3, respectively (see Sect. 5 and Schaerer et al. (2007) in agreement with this simple criterion. However, for the

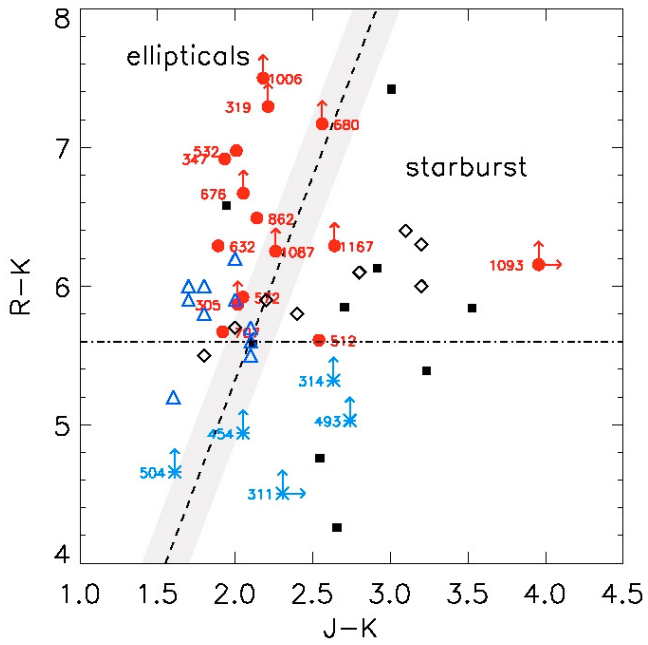

Fig. 3. Colour–colour plot of EROs found in Abell 1835 and AC114. Blue stars indicate objects classified as ERO – based on a 3σ non- detection (see Richard et al. 2006; Schaerer et al. 2007). Black diamonds show EROs found by Takata et al. (2003) in the vicinity of SCUBA source SMM J0452-0301. Black squares mark IEROs in the HUDF (Yan et al. 2004), and blue triangles show EROs found in the MUNICS survey (Longhetti et al. 2005). The dashed line shows the separation between old passive galaxies and dusty starbursts, according to Pozzetti & Mannucci (2000). The shaded area represents the gap between the ERO populations (≈0.3 mag). Arrows indicate the $R - K_s$ or $J - K_s$ colour to be a lower limit due to the non-detection in R or J respectively (see Tables 2 and 3).

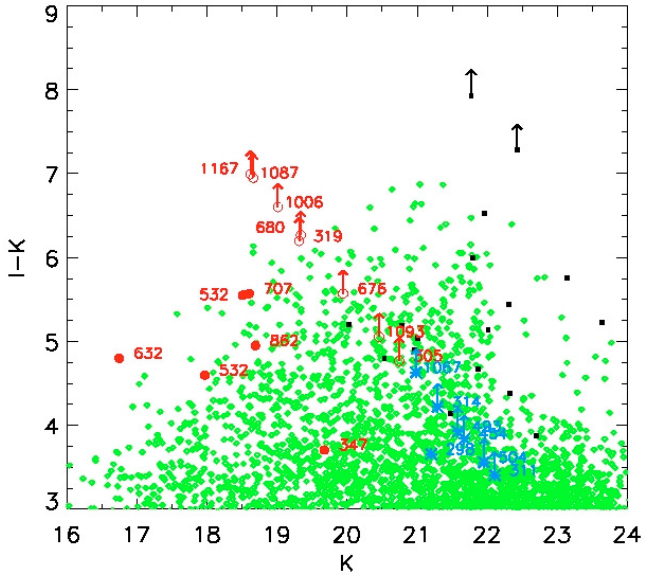

Fig. 4. $I - K$ vs. K colour–magnitude diagram for our sample of EROs (red), IEROs in the HUDF (black, Yan et al. 2004) and EROs found in GOODS-MUSIC (green, Grazian et al. 2007). Blue stars identify the objects described in Richard et al. (2006) and Schaerer et al. (2007). Arrows mark upper limits, and open circles denote EROs without R-band detection.

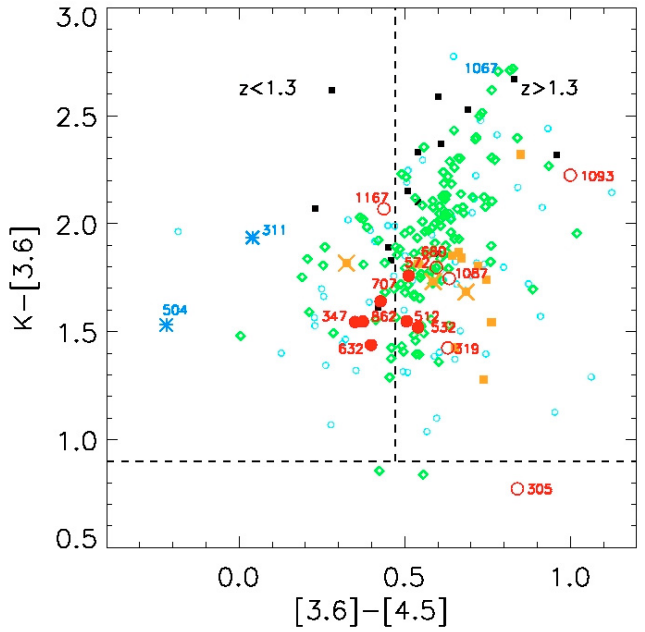

Fig. 5. K – [3.6] vs. [3.6]–[4.5] colour–colour diagram for extremely red galaxies. The red symbols represent our work. Filled: EROs with R-band detection; open: no R-band detection. We also includes the EROs from Richard et al. (2006) and Schaerer et al. (2007) (blue stars). The blue circles denote EROs selected on the basis of their red $(R - [3.6])_{\rm Vega} > 6.6$ or $(K - [3.6])_{\rm Vega} > 1.6$) colour (Wilson et al. 2004). Green and orange symbols show distant red galaxies (DRG) with $J - K > 2.3$ from Papovich (2006) and Labbé et al. (2005), respectively. Black squares indicate IEROs by Yan et al. (2004).

remaining objects with ([3.6]–[4.5]) close to the limit proposed by Wilson et al. (2004), there is only partial agreement for the separation of sources above or below $z = 1.3$ using the two methods, as can be seen by comparison with Table 7. More details on the photometric redshift determination of the EROs are given in Sect. 5 and Schaerer et al. (2007).

From a study of 24-μm selected objects Magliocchetti et al. (2007) suggest that objects with extreme 24-μm to R-band ratios of $\log F_{24}/F_R \lesssim -3$ are likely to be $z \sim 1.6$–3. All 6 MIPS-detected objects, except # 572 fall in this category. Both the colour criteria discussed above and SED modelling agree with this classification for #1093. For the 3 remaining objects (# 1006, # 1087, # 1167), a more complete SED fitting yields, however, photometric redshifts between ∼0.9 and 1.5. Such a simple criterion may thus overestimate the redshift of sources with extreme IR/optical flux ratios. However, since our objects have quite faint MIPS fluxes below the levels of ∼0.3 mJy discussed by Magliocchetti et al. (2007) and Houck et al. (2005), their criterion may be correct for more luminous sources.

4.4. Comparison of EROs with other galaxy populations

A significant overlap between different galaxy populations selected e.g. according to ERO, DRG, and other criteria is known to exist. In our case, e.g. 6 of our 15 EROs also satisfy the DRG selection criterion $J - K \geq 2.3$ as indicated in Tables 2 and 3, while 11 objects show the large 3.6 μm/z_{850} flux ratio used by Yan et al. (2004) to classify IRAC-selected objects (IEROs).

Considering e.g. the near-IR and IRAC colours shown in Fig. 5, we do not find a distinct difference to other populations: EROs (Wilson et al. 2004), DRGs (Papovich 2006), and IEROs (Yan et al. 2004). However, from this and from Fig. 6, it is clear that all sources without R-band detection lie in the outer regions

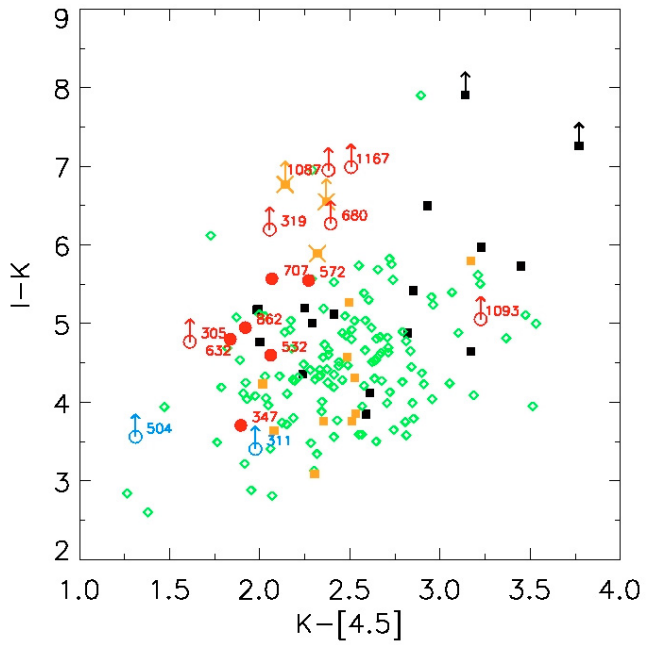

Fig. 6. Observed $I - K$ vs. $K - 4.5$ μm colour–colour diagram, same symbols as Fig. 5. Arrows indicate I-band non-detections, open circles non-detections in R.

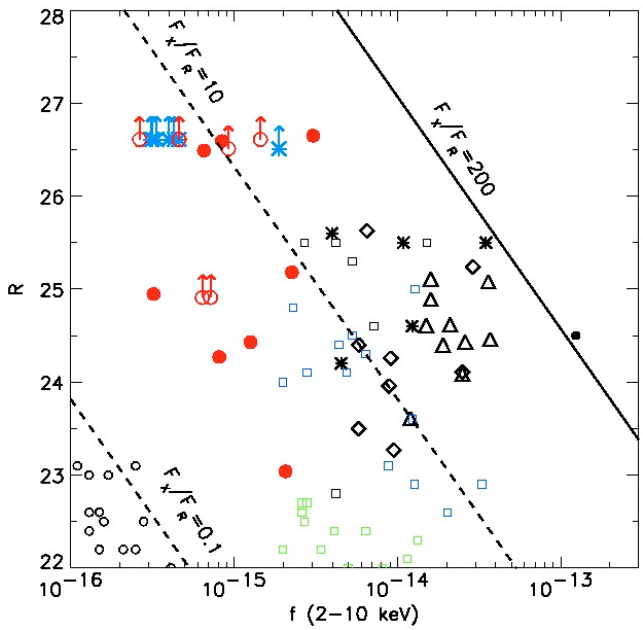

Fig. 7. R magnitude vs. 2–10 keV flux (in units of erg cm^{-2} s^{-1}) for our sample (red symbols, see Table 5), and for other X-ray emitting EROs. As none of our sources (red and blue symbols) was detected with Chandra, their Xray flux represents an upper limit. For a clearer plot, we have omitted the arrows in the horizontal direction. Triangles (black): Mignoli et al. (2004); diamonds (black): Brusa et al. (2005); small circles (black): Alexander et al. (2003); stars: Roche et al. (2003); large dot: XBS J0216-0435 (Severgnini et al. 2006; Della Ceca et al. 2004); open squares: Mainieri et al. (2002). The additional objects from Richard et al. (2006) and Schaerer et al. (2007) are indicated with blue stars. The two dashed lines define the region where unobscured type 1 AGNs typically lie (see Fiore et al. 2003; Maccacaro et al. 1988).

in these plots, indicating somewhat more extreme colours than DRGs, which are shared by some IEROs. Overall, most of them correspond to objects with very strong extinction as obtained from the SED analysis in Sect. 5.

In Fig. 6 we show the $I - K$ versus $K - 4.5$ μm colour, which Labbé et al. (2005) use to separate distant red galaxies (DRGs) from $z \sim 2.5$ Lyman break galaxies. All samples, DRGs (Labbé et al. 2005; Papovich 2006), IEROS (Yan et al. 2004) and our EROs (red) occupy the same colour space, with EROs without R-band detection again occupying the outer regions. We also include the ERO sample of Wilson et al. (2004). Three of the DRGs by Labbé et al. (2005) are thought to have old stellar populations, due to their very red $I - K$ colour. The 5 EROs in our sample, which have similar or even redder $I-K$ colours and comparable $K-[4.5]$ colours, were classified as "old evolved" galaxies due to their blue $J - K$ colour. However, from SED fitting (see below), we find that the majority of them are best fit with GRASIL spectral templates of very dusty star-forming galaxies, which is also supported by their detection at 24 μm. This shows that not all objects with such extreme $I - K$ colours are "old and dead" galaxies. In Schaerer et al. (2007), we have also shown that the bulk of the IEROs of Yan et al. (2004) are more likely dusty starbursts than old composite stellar populations. Detailed SED analysis including deep mid-IR observations may thus be needed to accurately determine the fraction of "old and dead" galaxies among red distant galaxies, as also pointed out by Kriek et al. (2006).

4.5. Starburst vs. AGN classification from X-rays

None of our EROs is detected in X-rays above the background of the galaxy cluster emission. However, thanks to the depth of the observations and the location of the objects away from the maximum cluster emission, the upper limits provide some interesting information on the nature of the EROs.

In Fig. 7 we plot the optical (R-band) flux or upper limits of our objects versus their X-ray flux limits. Also shown are other ERO samples from the literature (Mignoli et al. 2004; Brusa et al. 2005; Severgnini et al. 2006) and curves of constant X-ray to optical flux ratios; the range between $F_X/F_R = 0.1$ and 10 is typical of unobscured type 1 AGN. The majority of our objects detected in R are close to the border or outside of this region, indicating that they are probably not unobscured AGN. However, deeper X-ray observations might position our sources in the part of the plot occupied by those objects. For the other objects, this comparison relying on the R-band is not a strong constraint on their nature. More interesting is the comparison of the MIPS 24 μm flux with the X-rays, which is very useful for comparing AGN or starburst-dominated objects, as shown e.g. by Alonso-Herrero et al. (2004). These data are shown in Fig. 8, together with the regions of typical X-ray/mid-IR fluxes of local hard X-ray selected AGNs and local starbursts taken from Alonso-Herrero et al. (2004). Clearly the majority of 24 μm detected sources, i.e. 5 out of 7, have X-ray limits that exclude AGNs and are compatible with expectations from local starbursts. For the remaining objects, we cannot make a firm conclusion about their nature. However, no signature of an AGN is detected. In fact, if some of these objects turned out to be AGN, they would correspond to very faint AGN, given their reasonably well-established redshift. For our MIPS detected objects, the relatively small 8/24 μm flux ratio is also compatible with starburst-dominated objects (cf. Magliocchetti et al. 2007). We conclude that the bulk of our EROs are more likely to be starburst than AGN-dominated at near- to mid-IR wavelengths.

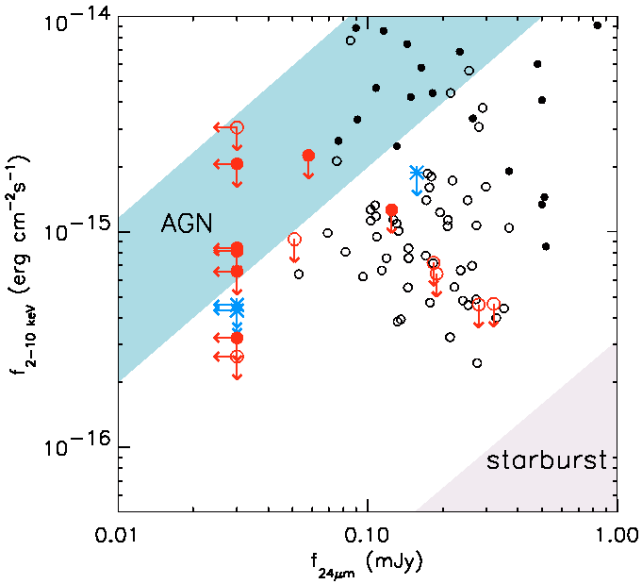

Fig. 8. The 24 μm flux vs. 2–10 keV X-ray flux (red: our work, filled: with R-band detection; open: no R-band detection). Arrows assign upper limits, both in X-ray and MIPs flux. Black symbols show X-ray selected sources with 24 μm counterparts in the CDF-S (Alonso-Herrero et al. 2006). Open black circles show sources not detected in hard X-rays. The Chandra 2–8 keV fluxes have been converted to 2–10 keV fluxes assuming a powerlaw with photon index $\Gamma = 1.4$. The blue shaded area is the extrapolation of the median hard X-ray-to-mid-IR ratios of local ($z < 0.12$) hard X-ray selected AGNs with mid-IR emission (Piccinotti et al. 1982). The purple area is the extrapolation of local starburst galaxies from Ranalli et al. (2003). The extrapolations were taken from Alonso-Herrero et al. (2004, 2006).

4.6. Magnification

Our only selection criteria is based on $R-K$ colour, which is not influenced by the magnification effects. However, to compare the number counts with other surveys, either in the field of lensing clusters (e.g. Smith et al. 2002) or large surveys (Simpson et al. 2006; Daddi et al. 2000; Smail et al. 2002) one has to correct for the magnification of the source flux and the dilution of the source plane. Magnification maps were derived following the procedure described in Richard et al. (2006) using the mass models of Abell 1835 (similar to Smith et al. 2005) and AC114 (Natarajan et al. 1998; Campusano et al. 2001). Given the position of each object (in terms of RA and Dec), we then determined the magnification factors. Table 6 lists the necessary correction if the source plane lies at redshift 0.5, 1.0, 1.5, 2.0, 3.0, and 7.0, respectively. As the field of Abell 1835 is positioned away from the cluster centre, most of the sources experience a relatively small correction. These magnification factors μ also have to be taken into account to compute absolute quantities, such as the stellar, SFR, etc., derived in Sect. 5.

4.7. Surface density

After correction for lensing and incompleteness, we obtained the surface density of EROs shown in Fig. 9. Although we used a slightly redder colour threshold than most authors, we compared our cumulative number counts with various other surveys. A comparable ERO sample in terms of environment is available from Smith et al. (2002), who studied 10 massive galaxy clusters at $z \sim 0.2$, including Abell 1835. However, the single ERO detected there has a colour of $R-K = 5.3$ and so does not satisfy our colour threshold, while even the brightest of our EROs in Abell 1835 (#532 $K = 17.97$) is not part of this sample. The explanation lies in both the smaller field size of the UKIRT camera (1.5 arcmin) and the centring of the field on the central cluster galaxy. As a result, EROJ140057+0252.4 (see Smith et al. 2002) lies at the very edge of our image, which we excluded due to the low signal-to-noise. The bright incompleteness limits (80% at $20.6^{\rm mag}$) in Smith et al. (2002) might be responsible for their non-detection of our faintest objects. The largest ERO survey, using the UKIDSS Ultra Deep survey, has been released recently by Simpson et al. (2006). However, a comparison is only possible for now at brighter magnitudes, $K < 20.1$.

Figure 9 shows the cumulative surface density of $R-K_{\rm s} \geq 5.6$ EROs in comparison with the samples of Smith et al. (2002) and Simpson et al. (2006) ($R-K > 5.3$ and $R-K > 6$). Up to $K = 20.5^{\rm mag}$, our number counts are slightly lower than those found by Smith et al. (2002) and Smail et al. (2002) but agree well within the 1σ error bars. Our lower number counts are also to be expected due to the redder colour threshold. We estimate the cumulative surface density of EROs at $K_{\rm s} \leq 20.5$ with (0.97 ± 0.31) arcmin^{-2}, compared to (1.16 ± 0.17) arcmin^{-2} and (0.50 ± 0.11) arcmin^{-2} by Smith et al. (2002) for $R-K \geq 5.3$ and $R-K \geq 6.0$ (up to the same K-limit). The number counts increase only slightly for fainter magnitudes, up to (1.36 ± 0.36) arcmin^{-2} at $K_{\rm s} \leq 22.0$.

The slope of $N(\geq K) = 10^{\alpha K}$ for our sample is $\alpha = 0.78 \pm 0.03$ for $K < 20.0$, compared to $\alpha = 1.05 \pm 0.05$ from Daddi et al. (2000) and $\alpha = 1.04 \pm 0.05$ for Smith et al. (2002). This slope decreases for fainter magnitudes ($20 < K < 22$) to $\alpha = 0.11 \pm 0.01$. Such a break in the cumulative number counts at $K \sim 19$–20 has been observed in various surveys (Smith et al. 2002; Daddi et al. 2000), although the actual values for α are found to be higher by a factor of ~2–3 in (Smith et al. 2002; Daddi et al. 2000) at fainter magnitudes ($K > 20.5$). This flattening could be caused by the absence of evolved ellipticals with fainter magnitudes.

The preliminary results from UKIDSS UDS EDR (Simpson et al. 2006) ($K \leq 20.15$) show much higher number counts than any other survey (e.g. Daddi et al. 2000; Smail et al. 2002; Smith et al. 2002). The authors attribute this result partly to the use of different filters and apertures.

5. Analysis of the observed SED

5.1. SED-fitting method

To analyse the observed SEDs quantitatively we follow the procedures outlined in Schaerer & Pelló (2005) and described in detail in Schaerer et al. (2007). We only briefly summarise the main points here.

The photometry in all bands except 24 μm with MIPS has been used. To take uncertainties in absolute flux calibrations between different instruments into account, we adopted a minimum photometric error of 0.1 mag in most computations. We used an updated version of the *Hyperz* code from Bolzonella et al. (2000) to constrain the redshift, stellar population properties (age, star formation history), and extinction of the galaxies studied in this paper. To do so we used in particular a large library of synthetic, empirical, and semi-empirical spectral templates. The templates are gathered into the following 4 groups:

1) Bruzual & Charlot plus Coleman et al. (1980) empirical templates galaxies of all Hubble types (hereafter named BC or BCCWW group). The theoretical Bruzual models

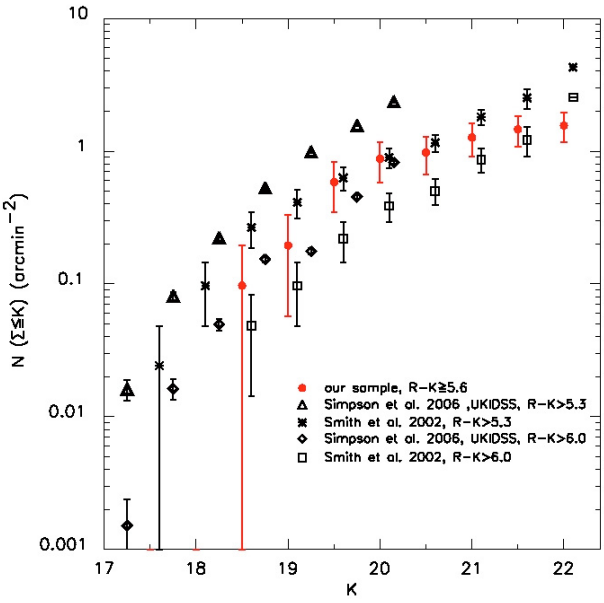

Fig. 9. Cumulative surface density of our sample ($R - K_s \geq 5.6$) after correcting for amplification (assuming a source plane at $z_s = 1.5$) and incompleteness. We also include the ERO sample ($R - K \geq 5.3$ and 6.0) of Smith et al. (2002) found in the fields of 10 massive galaxy cluster lenses and EROs found by Simpson et al. (2006) in the UKIDSS Ultra Deep Survey Early Data Release ($R - K \geq 5.3$).

(Bruzual & Charlot 2003), taken here for solar metallicity, include various star formation histories representative of different Hubble types. The IMF adopted in these models is the Miller-Scalo IMF from 0.1 to 125 $M_\odot$.

2) Starburst SEDs from Schaerer (2002, 2003) models at different metallicities extended up to ages of 1 Gyr and considering instantaneous bursts or constant star formation (hereafter s04gyr group). These models assume a Salpeter IMF from 1 to 100 $M_\odot$.
3) Empirical or semi-empirical starburst, ULIRG, and QSO templates. We used starburst templates from the Calzetti et al. (1994) and Kinney et al. (1996) atlas and the HST QSO template of Zheng et al. (1997). To also include more obscured objects, we added UV-to-millimeter band templates of EROs, ULIRGS, starburst, and normal galaxies (HR 10, Arp 220, M 82, NGC 6090, M 51, M 100, NGC 6949) from fits of GRASIL models to multi-wavelength observations Silva et al. 1998, named GRASIL group). This template group will be used in particular to predict mid-IR to sub-mm fluxes, and hence to estimate total bolometric luminosities, after fitting the optical to 8 μm part of the spectrum. The main free parameters we considerd are the spectral template (among a group), redshift z , and (additional) extinction (A_V) assuming a Calzetti et al. (2000) law. To increase the diversity of empirical or semi-empirical templates and to allowed for possible deviations from them, we also allow for an additional reddening. From the luminosity distance of the object or, if templates generated by evolutionary synthesis models are used, by scaling the template SED to the observed absolute fluxes, we obtained the absolute scaling for properties such as stellar mass or the star formation rate (SFR). In some cases we also used the bolometric luminosity computed from a GRASIL template to determine the SFR. Finally, the absolute quantities must also be corrected for the effects of gravitational lensing. The magnification factors listed in Table 6 are used for this purpose.

5.2. Results

5.2.1. Abell 1835

The SED fits and the derived properties for the optical dropout objects #305 (1), #311 (17), #314 (11), #454 (10), #493 (3), #504 (4), and #1093 (2), corresponding to the objects of Richard et al. (2006) with IDs in brackets, have already been discussed in depth in Schaerer et al. (2007). In the case of #1093 (2), the known sub-mm source SMMJ14009+0252, this also includes the SCUBA measurements by Ivison et al. (2000). We therefore limit the discussion here to the new objects in this field, i.e. #319, #347, #532, and #676. A summary of their derived properties is given in Table 7. For completeness and comparison, the derived properties of the objects from Schaerer et al. (2007) are listed at the bottom of this table. Note that the stellar masses have been corrected by $(1 + z)^{-1}$ to eliminate an error in the absolute scaling found in Schaerer et al. (2007). In contrast to the degeneracies found for many of the objects discussed in Schaerer et al. (2007), the photometric redshifts of the "new" objects show all well-defined best fits at low-z redshifts, $z \sim 0.9$ to 2.5. Object #319, one of the two newly identified I drop-outs, has the highest photometric redshift, $z_{\rm fit} \sim 2.4$–2.5, which is well-constrained by the "curvature" measured in the IRAC bands due to the stellar peak at 1.6 μm (restframe). Except possibly for #319, none of these objects are detected with MIPS at 24 μm.

Object #319 is best-fitted without extinction and with templates of elliptical galaxies or maximally old simple stellar populations (bursts). From SED fitting, this object is thus best characterised as "elliptical" in agreement with its empirical classification (Fig. 3). However, these SEDs are not able to explain the 24 μm flux.

The three remaining objects all clearly indicate dust, younger ages, and short star formation histories ("bursts"), although they would be classified as "ellipticals" according to their $(R - K)$ vs. $(J - K)$ colours (see Fig. 3). The estimated stellar masses of all these objects are between $M_\star \times \mu \sim 3 \times 10^{10}$ and 10^{12} $M_\odot$ with small magnification factors μ.

5.2.2. AC114

Using the templates from the BCCWW and s04gyr groups, all except one object have best-fit redshifts of $z_{\rm fit} \sim$ 1–2.6 (see Table 7). The exception is the R-dropout #1087, whose SED shows a very rapid and strong decline between the near-IR and optical bands, which is better fit with a Lyman-break than with a Balmer break. Formally its best photometric redshift is thus $z_{\rm fit} \sim 7$, but given the brightness of this object at near-IR and Spitzer bands, the high-z solution is extremely unlikely. Using the semi-empirical GRASIL templates the best fit is found at $z_{\rm fit} \sim 0.9$. This solution also naturally explains the observed 24 μm flux of this object, as shown in Fig. 10. For #862 the best fit with the BCCWW and s04gyr templates is found at $z_{\rm fit} \sim 1.1$, where GRASIL templates yield a somewhat lower redshift of ~0.6 retained in the table.

For 4 objects (#512, #632, #680, #707), the SED fitting indicates relatively small amounts of extinction ($A_v \lesssim 0.6$). Interestingly these correspond precisely to all the objects that are not detected at 24 μm. From their star-formation history (all burst-like) and their low (but not zero?) extinction, these objects resemble ellipticals, in agreement with their empirical classification. For the brightest of all our EROs, #632, we obtained different solutions with the BC and S04gyr templates respectively, namely $z_{\rm fit} \sim 1.3$ (2.5), ages of 4.5 (2.6) Gyr, and little or no

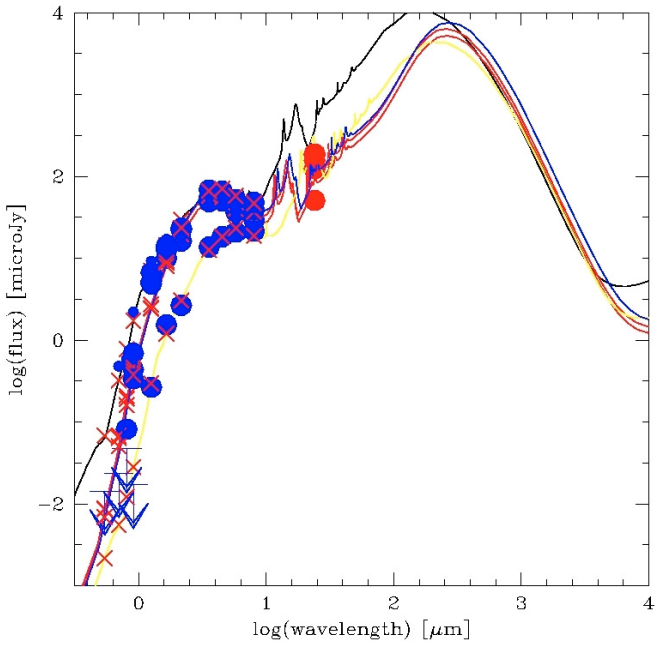

Fig. 10. SED fits with GRASIL templates for selected AC114 objects. Black: #572; red: #1006, #1087; yellow: #1067 (highest-z); blue: #1167. Sub-mm data (APEX/LABOCA) for this southern cluster are being aquired.

extinction, $A_v \sim 0.6$ (0.). The estimated stellar masses of these objects are between $M_\star \times \mu \sim 6. \times 10^{10}$ and 10^{12} $M_\odot$.

The remaining objects, all also detected at 24 μm, all show clear evidence of substantial extinction. In Table 7 we list their properties derived from fits with the GRASIL templates. The best fits are found with the M 51 or M 82 templates requiring, however, additional extinction in 5 out of 6 cases. The predicted 24 μm fluxes, not included in the SED modelling, agree well with the observations, except maybe for 572 whose MIPS flux is somewhat overestimated (see Fig. 10). In conclusion, for 572, 862, 1006, 1087, and 1167, all indications (SED fitting and MIPS detections) consistently confirm the dusty low-z (~0.9 to 2 or maybe 2.5) starburst nature of these objects. This shows the limitations of empirical diagrams, which would e.g. clearly classify three of them as ellipticals (cf. Fig. 3). As already mentioned above, our conclusion also does not support the explanation of objects with such extreme $I - K$ colours (cf. Fig. 6) as "old and dead galaxies" as proposed by Labbé et al. (2005) for galaxies at redshift $z > 2$.

The star formation rates estimated for these dusty objects from the bolometric luminosity of the GRASIL model fit are between $SFR \sim 15$ and 120 $M_\odot$ yr^{-1}, after correction for lensing. Their bolometric luminosities classify them in the range of luminous infrared galaxies (LIRG) with $L_{\rm bol} > 10^{11}$ $L_\odot$.

5.3. Discussion

As we can see from Table 7, the properties of our EROs span a rather wide range in extinction, stellar age, and stellar mass. The properties and their range are quite similar to those determined for DRGs by Förster-Schreiber et al. (2004) and for the IEROs of Yan et al. (2004) in Schaerer et al. (2007). However, in our sample we find some extreme objects in terms of colours, for which the SED modelling quite clearly indicates very high extinction ($A_V \sim 3$ and higher), which is not found in the DRG samples of Förster-Schreiber et al. (2004) and Papovich (2006). According to our analysis (see Schaerer et al. 2007) some IEROs of Yan et al. (2004) also show such high extinction.

6. Summary and conclusions

We have combined new ACS/HST, Spitzer (IRAC and MIPS guaranteed time), and the optical and near-IR observations of Richard et al. (2006) of two well-known lensing clusters, Abell 1835 and AC114, to study extremely red galaxies (EROs) in these fields. New and archival X-ray observations with ACIS/Chandra were also obtained for these clusters.

Using a standard $R - K \geq 5.6$, criterion we found 6 and 9 EROs in Abell 1835 and AC114, respectively. Several (8) of these objects are undetected up to the I and/or z_{850} band, and so are "optical" drop-out sources. Three of them, already identified earlier by Richard et al. (2006), were discussed in detail in Schaerer et al. (2007).

We have discussed the empirical properties of these EROs and compared them to other samples in the literature. We also undertook SED modelling based on a modified version of the *Hyperz* photometric redshift code and using a large number of spectral templates, including also very dusty galaxies. The main results can be summarised as follows:

- Among our EROs we find 3 sources showing quite unusually red colours in $R - K$ and other colours. Few similar objects are found e.g. among the samples of IRAC-selected IEROs of Yan et al. (2004), EROs of Sawicki et al. (2005), and the DRGs of Labbé et al. (2005). Our source density is compatible with other counts from the literature.
- After correcting for lens amplification, we estimate a surface density of (0.97 ± 0.31) arcmin^{-2} for EROs with $(R - K \geq 5.6)$ at $K < 20.5$. We observe a significant flattening of the number count at $K \sim 20$, possibly the result of losing the contribution of bright evolved ellipticals to the overall ERO population.
- According to "empirical" and to *Hyperz* modelling, the photometric redshifts of most of our sources yield $z \sim 0.7$–1.5. Five of them are found at higher redshift ($z \sim 2$–2.5).
- According to simple colour-colour diagrams, the majority of our objects would be classified as hosting old stellar populations ("ellipticals"). However, there are clear signs of dusty starbursts for several among them. These objects correspond to the most extreme ones in $R - K$ colour.
- We found that some very red DRGs, which would be classified as old and dead galaxies according to other studies (e.g. Labbé et al. 2005), are instead very dusty starbursts, even (U)LIRGs, as also supported their mid-IR photometry. Estimates of the fraction of old and dead galaxies among red galaxies may thus need to be treated with caution.
- As in earlier studies, an overlap of different populations is found. Among our 15 EROs, six also classify as DRGs (40%). Twelve of 14 EROs (85%) with available IRAC photometry also fulfil the selection criteria for IRAC-selected IEROs of Yan et al. (2004). Objects that do not classify as IERO are also not DRGs; however, the reverse is not true. SED modelling shows that ~40% of the IEROs are luminous or ultra-luminous infrared galaxies ((U)LIRG).
- None of our objects were detected at X-rays above the cluster background emission, with upper limits typically of the order of $\sim(3$–$10) \times 10^{-16}$ ergs s^{-1}cm^{-2} in the 0.5–7.0 keV band. There is no indication of AGNs, although faint activity cannot be excluded for all objects. From mid-IR and X-ray data, 5 objects are clearly classified as starbursts.

Table 7. Derived/estimated properties for EROs in Abell 1835 and AC114. To correct the absolute quantities for gravitational magnification the appropriate magnification factors listed in Table 6 must be used. The data at the bottom of the table is from Schaerer et al. (2007) (Tables 5 and 6), except for the stellar mass, which has been corrected by $(1 + z)^{-1}$ to eliminate an error in that paper.

Object ID		Redshift $z_{\rm phot}$	extinction $A_{\rm v}$ [mag]	Best fit template	DM[a] [mag]	$M^{\rm rest}(K_{\rm s}) - 2.5\log(\mu)$ [mag]	Mass $\times\,\mu$[b] $M_\odot$	$SFR \times \mu$ $M_\odot\ {\rm yr}^{-1}$	Stellar age [Gyr]
Abell 1835:									
298		0.8–1.1	0	elliptical	43.65	–22.0			
319		2.4–2.5	∼0	burst	46.60	–26.4	3.3×10^{11}		2.3
347		1.1–1.2	1.6–2.2	burst	44.35	–24.4	$(3.1–4.4) \times 10^{10}$		0.5–1.0
532		1.3–1.4	0.4–2.0	burst	44.71	–26.4	$(3.0–4.6) \times 10^{11}$		1.0–3.5
676		∼1.4	1.4–1.8	burst	45.0	–24.8	$(3.3–3.8) \times 10^{10}$		0.4–0.7
AC114:									
512		2.4–2.6	0.4	burst	46.65	–25.2	4.3×10^{10}		0.7
572		∼1.2		M 82	44.65	–26.1		35.7	
632		∼1.3 (2.5)	0.6 (0.)	burst	44.76	–27.5	1.5×10^{12}		4.5 (2.6)
680		∼2.1	0.6	burst	46.12	–26.5	2.3×10^{11}		1.4
707		∼1.2	0.6	elliptical	44.63	–25.8			
862		∼0.6	+3.2	M 51	42.76	–24.2		10.6	
1006		∼0.9	+3.6	M 51	43.86	–25.4		30.5	
1067		∼2.0	+2.0	M 82	46.02	–26.0		205.5	
1087		∼0.9	+3.8	M 51	43.77	–25.6		34.2	
305	(1)	∼0.4 –1.5	?	Fits uncertain – see paper I					
311	(17)	∼0.7–0.8	∼3.8	burst	43.0	–21.7	$\sim 7.6 \times 10^9$?	∼0.9	? (see paper I)
504	(4)	∼1.2	0–1.6	burst/elliptical	44.60	–21.6	$\sim 7.7 \times 10^9$	∼5	0.7 to 4.5
1093	(2)	∼2.8–3	2.4–3	young burst	47.0	–27.7	$\sim 3.2 \times 10^{11}$	∼2100	<0.36
1167	(1)	∼1.3–1.6	∼1.6–2.8	burst	44.84	–26.4	$(0.6–1.1) \times 10^{12}$		∼0.9–4.5 Gyr
1167	(1)	∼1.0	+3.8	M 51	44.03	–25.9		∼48	
493	(3)	∼1.1	∼0.6–0.8	burst	44.4	–22.2	$\sim 2.4 \times 10^9$		0.5
454	(10)	∼1.2	∼1.8	burst	44.68	–22.9	$\sim 3.6 \times 10^9$		0.5
314	(11)	?							

[a] Distance modulus computed for minimum redshift; [b] estimated stellar mass (from scaling the SED fit or from $M^{\rm rest}(K_{\rm s})$ assuming $L_K/M = 3.2$, col. 8)

– Quantitative SED fitting for our objects shows that they cover a fairly wide range in properties, such as extinction, stellar age, mass, and SFR. The derived properties are quite similar to those of DRGs and IEROs, except for 5 extreme objects in terms of colours, for which a very high extinction ($A_{\rm V} \gtrsim 3$) is found. According to our analysis, some IEROs of Yan et al. (2004) also show such high extinction (see Schaerer et al. 2007). From the SED modelling, these 5 EROs are expected to be (U)LIRG, and their IR to sub-mm SED is predicted.

Understanding the links between these different galaxy populations and their evolutionary history still remains to be done.

Acknowledgements. We thank Andrea Grazian for providing us with the GOODS-MUSIC catalogues and Graham Smith for making their results available in electronic format.
Support from *ISSI* (International Space Science Institute) in Bern for an "International Team" is kindly acknowledged. Part of this work was supported by the Swiss National Science Foundation, the French *Centre National de la Recherche Scientifique*, and the French *Programme National de Cosmologie* (PNC) and *Programme National de Galaxies* (PNG).
This paper is based on observations collected at the European Space Observatory, Chile (069.A-0508,070.A-0355,073.A-0471), and the Canada-France-Hawaii Telescope operated by the National Research Council of Canada, the French Centre National de la Recherche Scientifique (CNRS) and the University of Hawaii, and the NASA/ESA Hubble Space Telescope operated by the Association of Universities for Research in Astronomy, Inc., the Spitzer Space Telescope, which is operated by the Jet Propulsion Laboratory, California Institute of Technology under NASA contract 1407, and the Chandra satellite. This research was supported in part by Chandra General Observer Program grant GO6-7106X.

References

Alexander, D. M., Vignali, C., Bauer, F. E., et al. 2002, AJ, 123, 1149
Alexander, D. M., Bauer, F. E., Brandt, W. N., et al. 2003, AJ, 126, 539
Alonso-Herrero, A., Pérez-González, P. G., Rigby, J., et al. 2004, ApJS, 154, 155
Alonso-Herrero, A., Pérez-González, P. G., Alexander, D. M., et al. 2006, ApJ, 640, 167
Bergström, S., & Wiklind, T. 2004, A&A, 414, 95
Bertin, E., & Arnouts, S. 1996, A&AS, 117, 393
Bolzonella, M., Miralles, J.-M., & Pelló, R. 2000, A&A, 363, 476
Brusa, M., Comastri, A., Daddi, E., et al. 2005, A&A, 432, 69
Bruzual, G., & Charlot, S. 2003, MNRAS, 344, 1000
Calzetti, D., Kinney, A. L., & Storchi-Bergmann, T. 1994, ApJ, 429, 582
Calzetti, D., Armus, L., Bohlin, R. C., et al. 2000, ApJ, 533, 682
Campusano, L. E., Pelló, R., Kneib, J.-P., et al. 2001, A&A, 378, 394
Cimatti, A., Daddi, E., di Serego Alighieri, S., et al. 1999, A&A, 352, L45
Cimatti, A., Pozzetti, L., Mignoli, M., et al. 2002, A&A, 391, L1
Coleman, G. D., Wu, C.-C., & Weedman, D. W. 1980, ApJS, 43, 393
Cowie, L. L., Gardner, J. P., Hu, E. M., et al. 1994, ApJ, 434, 114
Czoske, O., Kneib, J.-P., & Bardeau, S. 2003, in Conf. Ser., ed. S. Bowyer & C.-Y. Hwang (ASP), 301, 281
Daddi, E., Cimatti, A., Broadhurst, T., et al. 2002, A&A, 384, L1
Daddi, E., Cimatti, A., Pozzetti, L., et al. 2000, A&A, 361, 535
De Filippis, E., Bautz, M. W., Sereno, M., & Garmire, G. P. 2004, ApJ, 611, 164
Della Ceca, R., Maccacaro, T., Caccianiga, A., et al. 2004, A&A, 428, 383
Egami, E., Misselt, K. A., Rieke, G. H., et al. 2006, ApJ, 647, 922
Elston, R., Rieke, G. H., & Rieke, M. J. 1988, ApJ, 331, L77
Elston, R., Rieke, M. J., & Rieke, G. H. 1989, ApJ, 341, 80
Fazio, G. G., Hora, J. L., Allen, L. E., et al. 2004, ApJS, 154, 10
Ferguson, H. C., Dickinson, M., & Williams, R. 2000, ARA&A, 38, 667
Fiore, F., Brusa, M., Cocchia, F., et al. 2003, A&A, 409, 79
Fontana, A., Pozzetti, L., Donnarumma, I., et al. 2004, A&A, 424, 23
Förster-Schreiber, N. M., van Dokkum, P. G., Franx, M., et al. 2004, ApJ, 616, 40
Georgakakis, A., Hopkins, A. M., Afonso, J., et al. 2006, MNRAS, 140
Gilbank, D. G., Smail, I., Ivison, R. J., & Packham, C. 2003, MNRAS, 346, 1125

Graham, J. R., & Dey, A. 1996, ApJ, 471, 720
Grazian, A., Fontana, A., de Santis, C., et al. 2006, A&A, 449, 951
Grazian, A., Nonino, M., & Gallozzi, S. 2007, [arXiv:astro-ph/0701233]
Houck, J. C., & Denicola, L. A. 2000, in Astronomical Data Analysis Software and Systems IX, ed. N. Manset, C. Veillet, & D. Crabtree, ASP Conf. Ser., 216, 591
Houck, J. R., Soifer, B. T., Weedman, D., et al. 2005, ApJ, 622, L105
Hu, E. M., & Ridgway, S. E. 1994, AJ, 107, 1303
Im, M., Simard, L., Faber, S. M., et al. 2002, ApJ, 571, 136
Ivison, R. J., Smail, I., Barger, A. J., et al. 2000, MNRAS, 315, 209
Ivison, R. J., Smail, I., Frayer, D. T., Kneib, J.-P., & Blain, A. W. 2001, ApJ, 561, L45
Kauffmann, G., White, S. D. M., & Guiderdoni, B. 1993, MNRAS, 264, 201
Kinney, A. L., Calzetti, D., Bohlin, R. C., et al. 1996, ApJ, 467, 38
Kitzbichler, M. G., & White, S. D. M. 2006, MNRAS, 366, 858
Kriek, M., van Dokkum, P. G., Franx, M., et al. 2006, ApJ, 649, L71
Labbé, I., Huang, J., Franx, M., et al. 2005, ApJ, 624, L81
Longhetti, M., Saracco, P., Severgnini, P., et al. 2005, MNRAS, 361, 897
Maccacaro, T., Gioia, I. M., Wolter, A., Zamorani, G., & Stocke, J. T. 1988, ApJ, 326, 680
Magliocchetti, M., Silva, L., Lapi, A., et al. 2007, MNRAS, 375, 1121
Mainieri, V., Bergeron, J., Hasinger, G., et al. 2002, A&A, 393, 425
McCarthy, P. J. 2004, ARA&A, 42, 477
Mignoli, M., Pozzetti, L., Comastri, A., et al. 2004, A&A, 418, 827
Moustakas, L. A., Casertano, S., Conselice, C. J., et al. 2004, ApJ, 600, L131
Natarajan, P., Kneib, J.-P., Smail, I., & Ellis, R. S. 1998, ApJ, 499, 600
Papovich, C. 2006, New Astron. Rev., 50, 134
Pettini, M., Steidel, C. C., Adelberger, K. L., Dickinson, M., & Giavalisco, M. 2000, ApJ, 528, 96
Piccinotti, G., Mushotzky, R. F., Boldt, E. A., et al. 1982, ApJ, 253, 485
Pozzetti, L., & Mannucci, F. 2000, MNRAS, 317, L17
Pozzetti, L., Bruzual A., G., & Zamorani, G. 1996, MNRAS, 281, 953
Ranalli, P., Comastri, A., & Setti, G. 2003, A&A, 399, 39
Richard, J., Pelló, R., Schaerer, D., Le Borgne, J.-F., & Kneib, J.-P. 2006, A&A, 456, 861
Roche, N. D., Dunlop, J., & Almaini, O. 2003, MNRAS, 346, 803
Sawicki, M. 2002, AJ, 124, 3050
Sawicki, M., Stevenson, M., Barrientos, L. F., et al. 2005, ApJ, 627, 621
Schaerer, D. 2002, A&A, 382, 28
Schaerer, D. 2003, A&A, 397, 527
Schaerer, D., & Pelló, R. 2005, MNRAS, 362, 1054
Schaerer, D., Hempel, A., Egami, E., et al. 2007, A&A, 469, 47
Severgnini, P., Caccianiga, A., Braito, V., et al. 2006, A&A, 451, 859
Silva, L., Granato, G. L., Bressan, A., & Danese, L. 1998, ApJ, 509, 103
Simpson, C., Almaini, O., Cirasuolo, M., et al. 2006, MNRAS, 373, L21
Smail, I., Ivison, R. J., Blain, A. W., & Kneib, J.-P. 1998, ApJ, 507, L21
Smail, I., Owen, F. N., Morrison, G. E., et al. 2002, ApJ, 581, 844
Smith, G. P., Smail, I., Kneib, J.-P., et al. 2002, MNRAS, 330, 1
Somerville, R. S., Primack, J. R., & Faber, S. M. 2001, MNRAS, 320, 504
Somerville, R. S., Moustakas, L. A., Mobasher, B., et al. 2004, ApJ, 600, L135
Stern, D., Chary, R.-R., Eisenhardt, P. R. M., & Moustakas, L. A. 2006, AJ, 132, 1405
Swinbank, A. M., Bower, R. G., Smith, G. P., et al. 2007, MNRAS, 72
Takata, T., Kashikawa, N., Nakanishi, K., et al. 2003, PASJ, 55, 789
Tinsley, B. M., & Gunn, J. E. 1976, ApJ, 203, 52
Treu, T., Ellis, R. S., Liao, T. X., et al. 2005, ApJ, 633, 174
Werner, M. W., Roellig, T. L., Low, F. J., et al. 2004, ApJS, 154, 1
White, S. D. M., & Rees, M. J. 1978, MNRAS, 183, 341
Wilson, G., Huang, J.-S., Pérez-González, P. G., et al. 2004, ApJS, 154, 107
Yan, L., & Thompson, D. 2003, ApJ, 586, 765
Yan, H., Dickinson, M., Eisenhardt, P. R. M., et al. 2004, ApJ, 616, 63
Zheng, W., Kriss, G. A., Telfer, R. C., Grimes, J. P., & Davidsen, A. F. 1997, ApJ, 475, 469

Online Material

Table 1. Characteristics of the observations.

Filter[a]		$\lambda_{\rm eff}$[nm]		$t_{\rm exp}$[s]		Depth (1σ) [mag]		$C_{\rm AB}$[mag]	
Abell 1835	AC114	Abell 1835	AC114	Abell 1835	AC114	Abell 1835	AC114	Abell 1835	AC114
	U		365		20 000		29.1		0.693
	B		443		9000		29.0		–0.064
V		543	547	3750	20 000	28.1	28.5	0.018	0.022
R	R_{702}	664	700	5400	8300 (400)[b]	27.8	27.7 (26.1)[b]	0.246	0.299
I	I_{814}	817	801	4500	2070	26.7	26.8	0.462	0.439
z_{850}		911		9110	9184	27.7	27.7	0.540	
SZ		1070		21 960		26.9		0.691	
J		1259		6480	6480	25.6	25.5	0.945	
H		1656		13 860	12 860	24.7	24.7	1.412	
$K_{\rm s}$		2167		18 990	18 990	24.7	24.3	1.871	
3.6		3577		2400	2400	∼0.2 μJy		2.790	
4.5		4530		2400	2400	∼0.3 μJy		3.249	
5.8		5788		3600	2400	∼1.2 μJy		3.737	
8.0		8045		3600	2400	∼1.5 μJy		4.392	
24.0		23 680		2700⋆	2700⋆	∼10.0 μJy			

[a] If only one filter name is given, than the same setup was used for both fields.
[b] For small fractions of the final R_{702} image, the total exposure time is only 400 s. For objects without R-band detection; we adjusted the detection limits accordingly (see Table 2).
⋆ The 24 μm integration time is as much as 3600 s within a ∼30″ wide strip crossing the cluster centre because of the way multiple data sets were taken.

Table 2. Optical and NIR photometry of EROs in Abell 1835.

ID	[b]	RA	Dec	V 3σ	R 3σ	I 3σ	z_{850} 3σ	SZ 3σ	J 3σ	H^c 3σ	K_s^c 3σ	DRG [d]	IERO [e]
305	(1)	14:00:58.264	2:50:27.15	>26.9	>26.6	>25.5	25.70 ± 0.07	24.44 ± 0.27	22.76 ± 0.16	22.40 ± 0.08	20.74 ± 0.02	no	yes
319[a]		14:01:06.059	2:50:29.53	>26.9	>26.6	>25.5	25.67 ± 0.10	22.32 ± 0.07	21.53 ± 0.09	20.64 ± 0.03	19.31 ± 0.01	no	yes
319[a]		14:01:06.059	2:50:29.53	>26.9	>26.6	>25.5	24.72 ± 0.08	22.32 ± 0.07	21.53 ± 0.09	20.64 ± 0.03	19.31 ± 0.01	no	yes
347		14:01:06.143	2:50:34.24	>26.9	26.59 ± 0.37	23.38 ± 0.18	23.45 ± 0.02	22.52 ± 0.04	21.61 ± 0.05	20.79 ± 0.02	19.67 ± 0.01	no	no
532		14:01:02.457	2:51:11.36	>26.9	24.95 ± 0.12	22.57 ± 0.06	22.12 ± 0.01	20.82 ± 0.01	19.98 ± 0.01	18.95 ± 0.00	17.97 ± 0.00	no	yes
676		14:01:07.781	2:51:35.51	>26.9	>26.6	>25.5	23.64 ± 0.05	22.20 ± 0.05	21.99 ± 0.12	21.08 ± 0.04	19.94 ± 0.01	no	ND
1093	(2)	14:00:57.530	2:52:49.34	>26.9	>26.6	>25.5	>26.5	24.08 ± 0.26	>24.4	21.78 ± 0.06	20.45 ± 0.02	yes	yes
EROs listed in (Richard et al. 2006) and (Schaerer et al. 2007) based on a 1σ detection threshold in the used R-band													
311	(17)	14:01:04.995	2:50:27.73	>26.9	>26.6	>25.5	>26.5	>25.7	>24.4	23.51 ± 0.16	22.11 ± 0.03	yes	yes
314	(11)	14:01:06.163	2:50:28.38	>26.9	>26.6	>25.5	>26.5	>25.7	23.92 ± 0.36	23.49 ± 0.18	21.29 ± 0.03	yes	ND
454	(10)	14:00:59.876	2:50:57.90	>26.9	>26.6	>25.5	25.56 ± 0.11	24.00 ± 0.12	23.72 ± 0.26	23.36 ± 0.13	21.67 ± 0.03	no	ND
493[a]	(3)	14:01:01.470	2:51:03.93	>26.9	>26.6	>25.5	24.06 ± 0.07	23.78 ± 0.10	24.32 ± 0.47	22.55 ± 0.07	21.58 ± 0.03	yes	ND
493[a]	(3)	14:01:01.470	2:51:03.93	>26.9	>26.6	>25.5	25.31 ± 0.13	23.78 ± 0.10	24.32 ± 0.47	22.55 ± 0.07	21.58 ± 0.03	yes	ND
504	(4)	14:01:01.719	2:51:05.56	>26.9	>26.6	>25.5	25.48 ± 0.14	24.44 ± 0.15	23.56 ± 0.18	22.90 ± 0.07	21.95 ± 0.03	no	no

[a] Objects may appear twice because of multiple ACS detections (#319 and #493). [b] The number in brackets behind the ID number refers to the ID in Richard et al. (2006). [c] The magnitude errors given here are solely based on the Sextractor output and are likely underestimated (cf. text). Errors of 0.00 occur due to rounding effects. [d] This column indicates whether the object satisfies the DRG criterion $J - K > 2.3$. [e] Several objects can be classified as IERO as described by Yan et al. (2004) ($f_\nu(3.6\,\mu\mathrm{m})/f_\nu(z_{850}) > 20$). ND stand for no data available, possibly due to blending.

Table 3. Same as Table 2 for the EROs in AC114.

ID		RA	Dec	V 3σ	R 3σ	I 3σ	z_{850} 3σ	J 3σ	H 3σ	K_s 3σ	DRG	IERO
512		22:58:53.278	–34:49:02.48	>27.3	26.49 ± 0.12	[c]	26.31 ± 0.11	23.42 ± 0.15	21.76 ± 0.03	20.88 ± 0.02	yes	yes
572		22:58:45.761	–34:48:47.89	>27.3	24.43 ± 0.02	24.06 ± 0.12	22.51 ± 0.02	20.56 ± 0.02	19.42 ± 0.01	18.51 ± 0.00	no	yes
632		22:58:46.664	–34:48:31.89	>27.3	23.04 ± 0.01	21.55 ± 0.03	20.57 ± 0.01	18.64 ± 0.01	17.64 ± 0.00	16.75 ± 0.00	no	no
680		22:58:51.361	–34:48:26.90	>27.3	26.65 ± 0.13	>25.6	24.51 ± 0.07	21.90 ± 0.05	20.30 ± 0.01	19.34 ± 0.01	yes	yes
707		22:58:51.357	–34:48:18.55	>27.3	24.27 ±0 .03	24.17 ± 0.15	22.36 ± 0.02	20.52 ± 0.02	19.50 ± 0.01	18.60 ± 0.00	no	no
862		22:58:52.560	–34:47:56.54	>27.3	25.18 ± 0.04	23.64 ± 0.09	22.66 ± 0.02	20.83 ± 0.02	19.72 ± 0.01	18.69 ± 0.00	no	yes
1006		22:58:49.014	–34:47:26.53	>27.3	>27.7	>25.6	24.27 ± 0.04	21.19 ± 0.04	20.00 ± 0.01	19.01 ± 0.01	yes	ND
1087		22:58:51.727	–34:47:07.85	>27.3	>24.9[a]	25.5 ± 0.33	23.77 ± 0.04	20.92 ± 0.03	19.63 ± 0.01	18.66 ± 0.00	yes	yes
1167	(1)	22:58:49.775	–34:46:55.00	>27.3	>24.9[b]	>25.6	24.55 ± 0.07	21.26 ± 0.04	19.75 ± 0.01	18.62 ± 0.00	yes	yes

[a] Since the effective exposure time is lower in this region, a lower detection limit has been applied (cf. Sect. 4.1). [b] Object located where two regions with different exposure times meet. The detection l imit for the shorter exposure was adopted (see Sect. 4.1 for more details). [c] Object lies outside of image

Table 4. IRAC and MIPS fluxes for EROS found in Abell 1835 and AC114.

ID		3.6 μm	4.5 μm	5.8 μm	8.0 μm	24 μm
Abell 1835		μJy	μJy	μJy	μJy	μJy
305	(1)	2.9 ± 0.2	4.0 ± 0.2	< 3.6	<4.5	<30.
319		19.7 ± 0.4	22.5 ± 0.4	26.5 ± 1.7	18.1 ± 1.6	272 ± 9*
347		15.7 ± 0.3	13.9 ± 0.3	< 3.6	8.0 ± 1.5	< 30.
532		73.6 ± 0.3	75.3 ± 0.3	51.3 ± 1.5	37.1 ± 1.5	< 30.
676			blended			
1093	(2)	14.4 ± 0.2	23.0 ± 0.3	37.6 ± 1.5	50.9 ± 1.6	320 ± 11
311	(17)	2.4 ± 0.2	1.6 ± 0.2	<3.6		<30.
314	(11)		blended			
454	(10)		blended			
493	(3)		blended			
504	(4)	1.9 ± 0.2	1.0 ± 0.3	<3.6		<30.
AC114						
512		5.2 ± 0.2	5.3 ± 0.2	7.1 ± 1.2	<4.5	<30.
572		56.0 ± 0.3	57.4 ± 0.3	51.0 ± 1.3	43.8 ± 1.4	124.9 ± 7.9
632		210.8 ± 1.0	194.6 ± 0.9	131.2 ± 1.7	92.1 ± 2.2	<30.
680		27.0 ± 0.2	29.9 ± 0.3	31.8 ± 1.1	16.9 ± 1.4	<30.
707		46.2 ± 0.3	43.8 ± 0.3	25.1 ± 1.2	23.2 ± 1.4	<30.
862		39.0 ± 0.2	35.2 ± 0.3	28.7 ± 1.1	22.5 ± 1.4	58.0 ± 10.4
1006		blended		36.0 ± 1.2	27.5 ± 1.4	51.0 ± 7.9
1087		48.2 ± 0.2	55.3 ± 0.3	44.0 ± 1.2	36.5 ± 1.5	183.7 ± 7.4
1167	(1)	67.3 ± 0.5	64.4 ± 0.5	50.3 ± 1.5	44.9 ± 2.2	189.0 ± 8.9

Table 5. X-ray flux limits for the EROs in Abell 1835 and AC114.

ID	(0.5–7.0 keV)		(2.0–10.0 keV)
Abell 1835	Γ = 1.0	Γ = 2.0	Γ = 1.4
305	3.14e-16	2.21e-16	2.64e-16
319	5.44e-16	3.85e-16	4.60e-16
347	9.98e-16	7.08e-16	8.43e-16
532	3.81e-16	2.70e-16	3.21e-16
676	1.71e-15	1.22e-15	1.45e-15
1093	5.47e-16	3.87e-16	4.63e-16
311	5.42e-16	3.85e-16	4.60e-16
314	3.72e-16	2.64e-16	3.16e-16
454	3.98e-16	2.81e-16	3.36e-16
493	4.72e-16	3.34e-16	3.99e-16
504	5.11e-16	3.61e-16	4.30e-16
AC114			
512	8.79e-16	4.52e-16	6.55e-16
572	2.37e-15	5.75e-16	1.26e-15
632	3.25e-15	9.74e-16	2.06e-15
680	4.32e-15	1.70e-15	3.05e-15
707	1.09e-15	5.58e-16	8.13e-16
862	3.05e-15	1.55e-15	2.26e-15
1006	1.25e-15	6.31e-16	9.25e-16
1087	9.72e-16	4.91e-16	7.19e-16
1167	8.63e-16	4.38e-16	6.40e-16

Table 6. Magnification factors μ from the lensing models of Abell 1835 and AC114 predicted for various source redshifts z_s.

ID		$z_s = 0.5$	$z_s = 1.0$	$z_s = 1.5$	$z_s = 2.0$	$z_s = 3.0$	$z_s = 7.0$
Abell 1835							
305	(1)	1.13	1.21	1.24	1.26	1.28	1.30
319		1.15	1.26	1.29	1.31	1.33	1.36
347		1.17	1.28	1.32	1.34	1.36	1.39
532		1.33	1.60	1.71	1.77	1.83	1.91
676		1.34	1.62	1.75	1.81	1.89	1.98
1093	(2)	1.43	1.82	1.99	2.09	2.20	2.34
311	(17)	1.17	1.28	1.32	1.34	1.36	1.39
314	(11)	1.15	1.26	1.29	1.31	1.33	1.36
454	(10)	1.22	1.38	1.44	1.47	1.50	1.54
493	(3)	1.27	1.48	1.57	1.61	1.66	1.72
504	(4)	1.29	1.51	1.60	1.64	1.70	1.76
AC114							
512		1.60	2.74	3.47	3.97	4.61	5.63
572		1.32	1.71	1.88	1.97	2.06	2.19
632		1.70	3.03	3.84	4.39	5.06	6.07
680		1.65	3.03	4.01	4.74	5.75	7.56
707		1.60	2.71	3.40	3.86	4.45	5.36
862		1.31	1.69	1.85	1.94	2.04	2.16
1006		1.50	2.26	2.65	2.88	3.14	3.50
1087		1.20	1.42	1.51	1.56	1.61	1.66
1167	(1)	1.24	1.53	1.64	1.71	1.77	1.86